



# Locust bean gum as green and water-soluble binder for $\text{LiFePO}_4$ and $\text{Li}_4\text{Ti}_5\text{O}_{12}$ electrodes

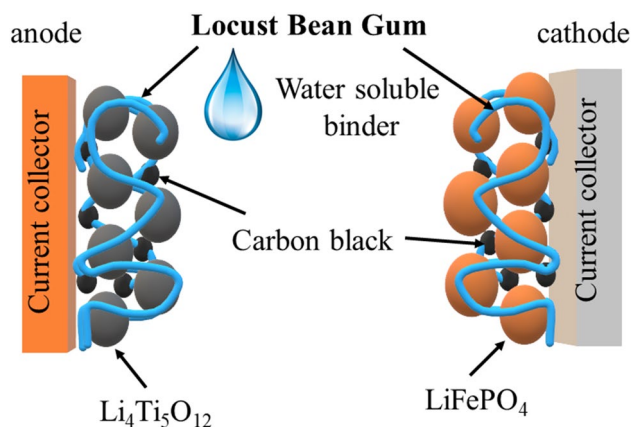
Paweł Jakóbczyk<sup>1,2</sup> · Michał Bartmański<sup>3</sup> · Ewelina Rudnicka<sup>1</sup>

Received: 17 May 2020 / Accepted: 10 October 2020  
© The Author(s) 2020

## Abstract

Locust Bean Gum (LBG, carob bean gum) was investigated as an environmentally friendly, natural, and water-soluble binder for cathode (LFP) and anode (LTO) in lithium-ion batteries (Li-ion). For the first time, we show LBG as an electrode binder and compare to those of the most popular aqueous (CMC) and conventional (PVDF) binders. The electrodes were characterized using TGA/DSC, the galvanostatic charge–discharge cycle test, cyclic voltammetry (CV), and electrochemical impedance spectroscopy (EIS). Thermal decomposition of LBG is seen to begin above 250 °C with a weight loss of about 60 wt% observed at 300 °C, which is sufficient to ensure stable performance of the electrode in a Li-ion battery. For CMC, weight loss at the same temperature is about 45%. Scanning electron microscopy (SEM) shows that the LFP–LBG system has a similar distribution of conductive carbon black particles to PVDF electrodes. The LTO–LBG electrode has a homogeneous dispersion of the electrode elements and maintains the electrical integrity of the network even after cycling, which leads to fast electron migration between LTO and carbon black particles, as well as ion conductivity between LTO active material and electrolyte, better than in systems with CMC and PVDF. The exchange current density, obtained from impedance spectroscopy fell within a broad range between  $10^{-4}$  and  $10^{-2}$  mA cm<sup>-2</sup> for the LTO|Li and LFP|Li systems, respectively. The results presented in this paper indicate that LBG is a new promising material to serve as a binder.

## Graphic abstract



**Keywords** Locust bean gum · Binder · Lithium-ion batteries · Anode · Cathode

## 1 Introduction

Lithium-ion batteries (LIBs) are continuously being developed and improved. Many papers presented attempt to increase their energy density, power, cyclability, or reduce

✉ Paweł Jakóbczyk  
pawel.jakobczyk@put.poznan.pl

Extended author information available on the last page of the article

their cost. It is also expected that these batteries will be environmentally friendly [1–4]. There have been many efforts to optimize the components of LiBs to broaden the range of their potential applications. Li-ion batteries are composed of anode and cathode electrodes separated by a separator soaked in an electrolyte. Both electrodes include an active material, a conductive agent, a current collector, and a polymeric binder. Although the content of the binder in electrodes is small (0.5–12 wt%), it is a key component of electrodes [5–8]. Binder materials have an influence on the physical structure and the whole electrical network integrity of electrodes [9]. They should be electrochemically stable in the requested potential window, guarantee good dispersion of the active material and the conducting agent and bind them with the current collector [10–12]. Binders may be divided into two groups. One is the organic-soluble group, including, e.g., poly(vinylidene difluoride) (PVDF) [13], polyaniline (PANI) [14], poly(methyl methacrylate) (PMMA) [15], and poly(vinylidene difluoride)-co-hexafluoropropylene (PVDF-HFP) [16]. The other group comprises binders which are either dissolved in water or their slurry with the active material and the conductive agent is prepared with the use of water. Examples are lithium or sodium salts of carboxymethyl cellulose (CMCLi, CMCNa) and its composite binder [17], polyvinyl acetate (PVAc) and chitosan, and its derivatives [4] xanthan gum [18] and sodium alginate [19, 20].

The most commonly used binder for LIBs is polyvinylidene difluoride (PVDF), which exhibits strong adhesion strength, chemical, and electrochemical stability. PVDF absorbs a large amount of liquid electrolyte, a property that has its advantages and disadvantages. An easy penetration of the electrolyte inside the electrode material causes a high interfacial area of the electrolyte/active material and effortless  $\text{Li}^+$  ions transport, while it also extends unwanted reactions. Besides, the soaked electrode material in the electrolyte swells and consequently loses contact between particles, causing increased resistance of the electrode [21]. Preparation of a cathode or an anode with PVDF as a binder requires organic solvents such as *N*-methylpyrrolidone (NMP), which is toxic and expensive. Additionally, at high temperatures, exothermic reactions take place between PVDF and lithium or lithiated graphite, which results in a rise of temperature and a threat to the safety of cell use [22]. To overcome these drawbacks it is necessary to find cheap, safe, and nontoxic binders as alternative candidates for PVDF. The most popular among them is the sodium salt of carboxymethyl cellulose (CMC). A number of papers present CMC as a promising binder in cathodes and in anodes [3, 17, 23]. Locust Bean Gum (LBG, carob bean gum) is a polysaccharide consisting of galactose and mannose units, thus it belongs to the group of galactomannans. LBG is extracted from the seeds of the carob tree (*Ceratonia siliqua*). The Mediterranean region is

abundant in these trees. They can be found in North Africa, South America, and Asia. The interest in this polysaccharide has recently increased in many fields. One of the main industries interested in LBG is the food industry. Locust bean gum is used as a food additive, in the European Union labeled as E-410. In addition, LBG is becoming more and more widely considered in biopharmaceutics as matrix forming material in tablets of oral administration of drugs [24]. LBG is a versatile material used for many applications, such as excellent stiffeners and stabilizers of emulsions. The absence of toxicity facilitates their use in the textile, pharmaceutical, biomedical, cosmetics, and food industries [25].

This manuscript investigates LBG as a new water-soluble binder for the cathode (LFP) and anode (LTO) in lithium-ion batteries (Li-ion). Electrodes were prepared with LBG, CMC, and PVDF. These electrodes were tested in the system with a lithium anode. Their thermal stability was characterized based on TGA/DSC measurement. The electrochemical battery performance for such prepared batteries were further investigated applying the galvanostatic charge–discharge cycle test. Cyclic voltammetry (CV) and electrochemical impedance spectroscopy (EIS) measurements were used to determine their polarization behavior, electrode reaction resistance, and kinetics characteristics. The obtained results for electrodes with LBG as a binder were compared to those of the most popular aqueous (CMC) and conventional (PVDF) binders.

## 2 Experimental

### 2.1 Materials

Lithium-iron phosphate ( $\text{LiFePO}_4$ , carbon coated, battery grade, BET surface area  $15.4 \text{ m}^2 \text{ g}^{-1}$ , Sigma-Aldrich), lithium titanate, spinel ( $\text{Li}_4\text{Ti}_5\text{O}_{12}$ , nanopowder < 200 nm particle size, Sigma-Aldrich), carbon black (CB, Fluka), poly(vinylidene fluoride) (PVDF,  $M_r = 180\,000$  Fluka), carboxymethylcellulose (CMC, Sigma-Aldrich), locust bean gum (LBG, Sigma-Aldrich) lithium foil (Sigma-Aldrich, 0.75 mm thick), *N*-methyl-2-pyrrolidinone (NMP, Fluka), solution of 1 M lithium hexafluorophosphate ( $\text{LiPF}_6$ ) in a mixture of ethylene carbonate (EC), and dimethyl carbonate (DMC) at the 1:1 volume ratio (Sigma-Aldrich) were used as received. The tested electrodes were prepared by casting the active material, the electronic conductor, and a binder slurry, in *N*-methyl-2-pyrrolidinone (NMP, Fluka) for PVDF binder or in water for CMC and LBG binders, on the current collector (diameter 12 mm) (solvents evaporated in vacuum at  $120^\circ\text{C}$ ). Three types of binders were used: PVDF, CMC, and LBG. In the case of the cathode,  $\text{LiFePO}_4$  was the active material, while  $\text{Li}_4\text{Ti}_5\text{O}_{12}$  was used in the anode. In both electrodes CB was used as an electronic conductor. The

ratio of components was  $\text{LiFePO}_4$ :CB:binder 85:10:5 (by weight) in the cathode and the ratio of  $\text{Li}_4\text{Ti}_5\text{O}_{12}$ :CB:binder was 85:5:10 (by weight) in the anode. The current collectors were aluminum foil (MTI Corporation, USA) and copper foil (Schlenk Metallfolien, Germany) for the cathode and anode, respectively.

The electrode contained typically 2–3 mg of the active material. A round-shaped metallic-lithium counter electrode was cut off from the metallic-lithium foil (surface area of  $1 \text{ cm}^2$ ).

## 2.2 Measurements

Electrochemical properties of the cells were characterized using electrochemical impedance spectroscopy (EIS), galvanostatic charging/discharging tests, and cyclic voltammetry. The cycling measurements were taken with the use of the ATLAS 0461 MBI multichannel electrochemical system (Atlas-Sollich, Poland) at different current rates (C/10–2C). The cells were cycled between 1.0 and 2.5 V for anode and 2.0 and 4.0 V for cathode. Cyclic voltammetry (CV) and impedance measurements were performed using the G1000 Multichannel System Gamry (Gamry Instruments, USA). Impedance spectra were obtained using a frequency response analyser at a frequency range of 100 kHz–10 MHz, at the open circuit potential (after lithiation to 1.2 V and 2.4 V for anode and cathode, respectively), and amplitude of 10 mV. Deconvolution of spectra was performed with the ZView software (Scribner Associates Inc., USA). Electrodes were separated by the glass microfiber GF/A separator (Whatmann, 0.4–0.6 mm thick), placed in an adapted 0.5" Swagelok® connecting tube. The cell was assembled in a glove box in the dry argon atmosphere. After electrochemical measurements, the cells were disassembled, the electrodes were washed with DMC and dried in the vacuum at room temperature, these operations were made in a dry argon atmosphere in a glove box. The morphology of the electrodes after and before the tests was observed under a scanning electron microscope (SEM, Tescan Vega 5153).

The adhesion of the electrode film to the copper (for anode) or aluminum (for cathode) foil was examined using microscratch-test technique on the Nanoindenter (NanoTest Vantage, Micromaterials, Wrexham, UK). The measure of adhesion was carried out on pristine and soaked–dried electrode–film samples. The soaked–dried electrodes were prepared by immersion of the electrodes in an electrolyte for lithium-ion batteries [1 M  $\text{LiPF}_6$  in EC–DMC (v/v = 1:1)] for 24 h at room temperatures. The swollen electrodes after soaking were washed with DMC and dried first in argon atmosphere for 2 h and next in the vacuum. The diamond indenter was used and the three independent microscratch-test with 2000  $\mu\text{m}$  full length and maximum applied force 200 mN on each specimens were performed. The distance

between each measurement was 1000  $\mu\text{m}$ . The adhesion force were examined based on the abrupt change in frictional force during the microscratch-test and confirmed by light microscopy (OLYMPUS BX51, Japan).

## 3 Results and discussion

### 3.1 Thermal stability

Thermal stability of different binders may be estimated from DSC/TG measurements. The tests were performed under nitrogen flow at a temperature increase rate of  $5 \text{ }^\circ\text{C min}^{-1}$ . Figure 1a–c presents the TGA/DSC graphs. The endothermic peaks corresponding to the evaporation of absorbed water appeared in the first part of curves for CMC (Fig. 1b)

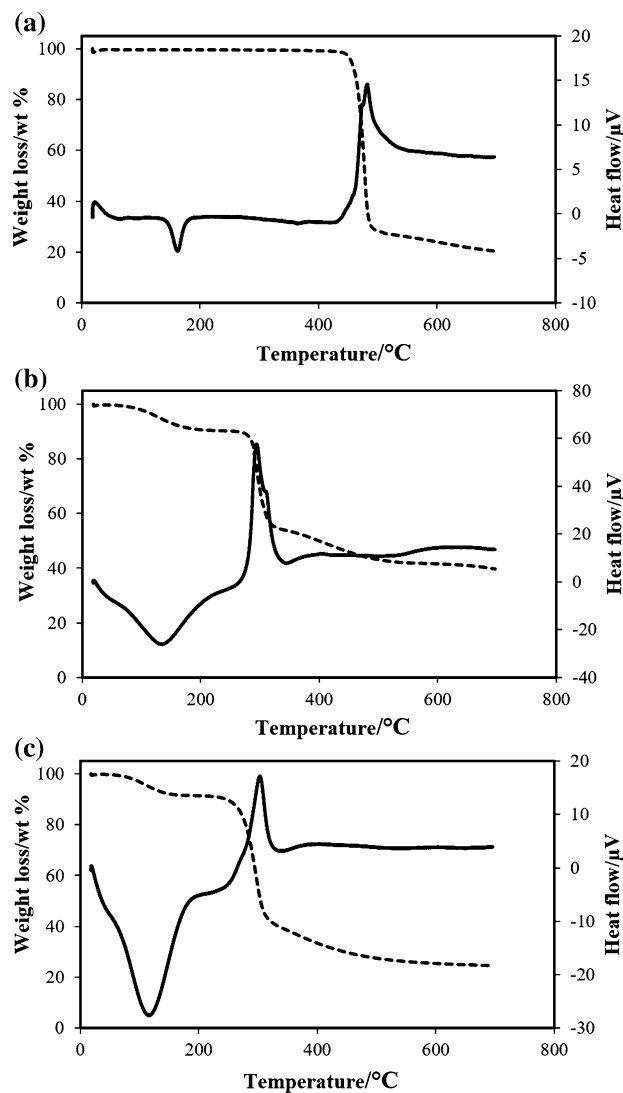


**Fig. 1** TGA and DSC curves for three binder materials under  $\text{N}_2$  at a heating rate of  $5 \text{ }^\circ\text{C min}^{-1}$  **a** PVDF, **b** CMC, and **c** LBG

and LBG (Fig. 1c). In the case of the DSC curve of PVDF a small peak may be observed at about 180 °C associated with binder melting. The thermal decomposition of CMC (Fig. 1b) and LBG (Fig. 1c) is seen to begin above 250 °C with a weight loss of approx. 45 wt% and 60 wt% observed at 300 °C for carboxymethyl cellulose and locust bean gum, respectively. PVDF shows (Fig. 1a) a decrease in weight at around 450 °C, which indicates its decomposition. The weight loss reached 68% at 485 °C. Above 480 °C only a slight weight loss is observed. Water-soluble binders have lower thermal stability, it is still sufficient to prepare electrodes, because they are dried at 120 °C. Lower thermal stability of LBG than PVDF does not exclude LBG from use in Li-ion batteries. Most devices powered by lithium-ion batteries work at temperatures below 100 °C [26–28].

### 3.2 SEM of LFP and LTO electrodes

The surface morphology of LFP and LTO electrodes with different binders before the cycling and after lithiation was investigated by scanning electron microscopy. The electrodes after cycling were extracted from the Swagelok-type cell inside the glove box, rinsed with dimethyl carbonate, and dried in an argon atmosphere. Figure 2 shows SEM images of the LFP cathode at a  $\times 10,000$  magnification. As shown in Fig. 2, the LFP–LBG electrode before the cycle test exhibited a relatively unfavorable distribution of conductive carbon black or even their agglomerate, similar to that of the most popular PVDF (Fig. 2c). By contrast, the LFP–CMC electrode showed a homogenous dispersion of LFP powder and conductive carbon black and maintained a

porous structure, indicating a homogenous distribution of LFP and carbon black particles. Galvanostatically charged/discharged LFP electrodes had a comparable morphology as before the process charging–discharging, but the surface of crystallites was covered with a solid electrolyte interphase (SEI) deposit (Fig. 2d–f).

As shown in Fig. 3 presenting SEM observations before the cycling test for LTO electrodes, the surface morphologies seem to be smooth and flat for the CMC and PVDF electrodes (Fig. 3b, c). In contrast, a porous structure was observed for the LTO–LBG electrode. After the discharging–charging–discharging process, the surface of electrodes was coated with a deposit layer.

The systems with LBG and PVDF as binders were not cracked. In the case of LTO–CMC, cracks of the surface were observed. It could be a reason for damage of the conducting matrix between active particles and carbon black particles. Also, the aluminum foil current collector may lose contact with the electrode and consequently resistance between the active material and the current collector may increase, thus leading to capacity fading. After the discharging–charging–discharging process, the LTO–LBG electrode retained integrity of the electrical network, the porous structure, and the homogenous dispersion of the ingredient materials such as LTO and carbon black. This provided a fast electron migration between the LTO particles and carbon black, as well as ion conductivity between the LTO active material and the electrolyte. In the case of the LTO–PVDF system less porosity is visible, which may result in reduced access to the active material and thus hinder migration of electrolyte ions in the electrode.

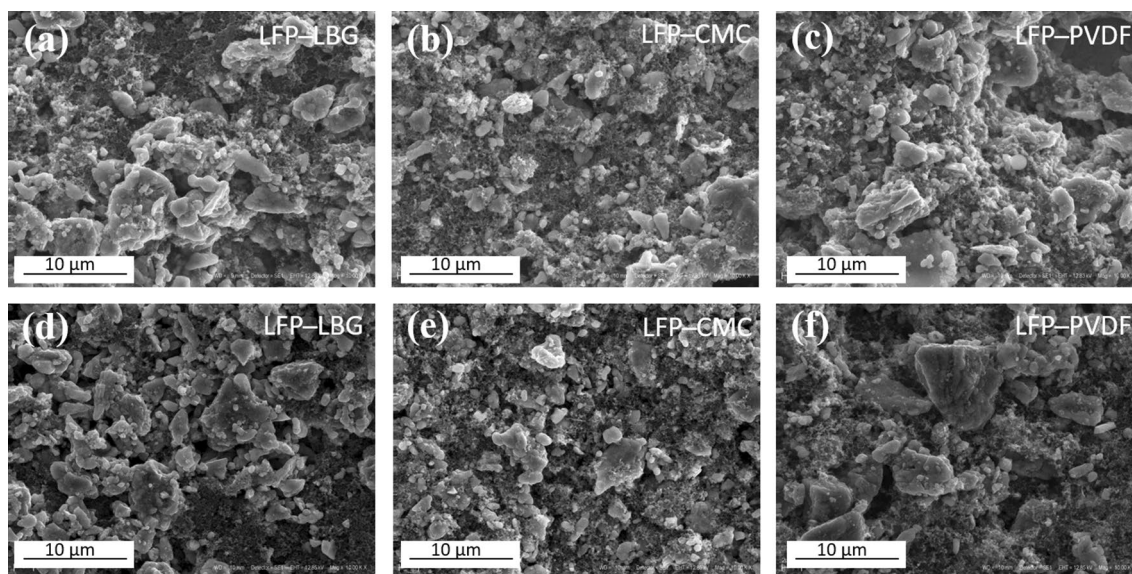


**Fig. 2** SEM images of LFP electrodes with LBG, CMC, and PVDF as binders before (a–c) and after (d–f) cycling processes, respectively (magnification  $\times 10,000$ )



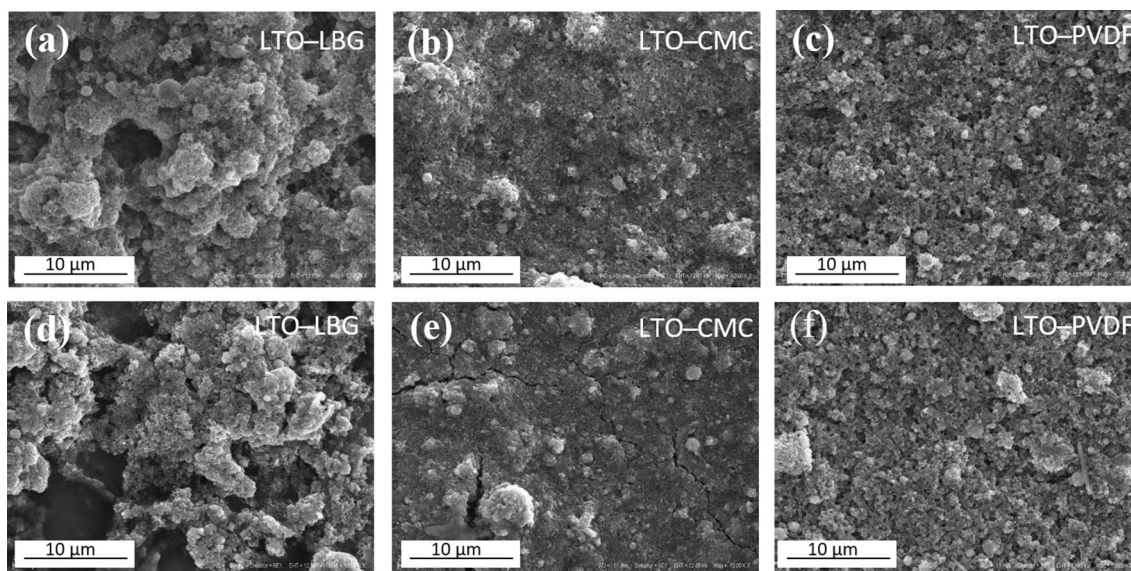


**Fig. 3** SEM images of LTO electrodes with LBG, CMC, and PVDF as binders before (a–c) and after (d–f) cycling processes, respectively (magnification  $\times 10,000$ )

**Table 1** Adhesion of the pristine and soaked–dried electrodes

	Critical force/mN	
	Pristine	Soaked–dried
LFP–PVDF	$24.01 \pm 4.05$	$15.86 \pm 1.93$
LFP–CMC	$17.64 \pm 1.39$	$48.46 \pm 5.78$
LFP–LBG	$20.51 \pm 13.49$	$29.48 \pm 12.19$
LTO–PVDF	$17.87 \pm 4.48$	$50.47 \pm 16.17$
LTO–CMC	$34.62 \pm 8.48$	$75.26 \pm 17.81$
LTO–LBG	$55.16 \pm 9.12$	$44.89 \pm 14.79$

### 3.3 Adhesion study

The adhesion results are shown in Table 1 and significant standard deviations confirm the reliability of the data obtained. The standard deviation is probably influenced by heterogeneous morphology on the sample surface. In the case of electrodes with CMC and LBG, an increase in adhesion was observed for soaked–dried electrode film, the largest in the case of LFP–CMC. The adhesion decreases for the soaked–dried LFP–PVDF electrode and increases for the LTO–PVDF electrode. The results suggest that the adhesion forces depend not only on the binder but also on the electrode material as well as on the combination of these two components. The highest values of adhesion for CMC do not reflect the best performance of the cell. The measured magnitude of the adhesion forces may be disturbed by the existing cohesive forces [29].

Figure 4 shows a single curve of the friction force from the normal force set during microaspiration for the pristine

(a) and dried–soaked (b) electrode. Sudden changes in the graph are the beginning of electrode delamination. To confirm the start of delamination, a photo of the scratch was made using optical microscopy (shown in Fig. 4). The appearance of light reflections of the substrate indicates the complete delamination of the electrode.

### 3.4 Cyclic voltammetry

The electrochemical stability of LFP and LTO electrodes with different binders are investigated by CV measurement from 2.5 to 4.5 V in Figs. 5 and 6, respectively. The CV curves of LFP–LBG, LFP–CMC, and LFP–PVDF electrodes at various scan cycles are shown in Fig. 5. The oxidation and reduction current peaks, corresponding to  $\text{Li}^+$  deinsertion and  $\text{Li}^+$  insertion, respectively, are presented during the forward and backward potential scanning [15, 30].

The LFP–LBG and LFP–CMC displayed similar CV profiles and the electrode using LBG, such as CMC, showed maintained electrochemical stability during 5 cycles, indicating that the LBG binder has no obvious impact on the LFP cathode electrochemical process (Fig. 5a). Potential differences in the fifth cycle between the redox peaks amounted to 0.17 V, 0.18 V, and 0.26 V for LBG, CMC, and PVDF, respectively. The LFP–LBG electrode showed a similar voltage difference to the LFP–CMC electrode, while it was lower than in the LFP–PVDF system. The LFP–LBG and LFP–CMC electrodes have lower peaks of oxidation and reduction in the first cycle than in the successive cycles. This is caused by the formation of the solid electrolyte interphase (SEI) layer enhancing charge transfer during lithium ions

**Fig. 4** Single microscratch-test curve with light microscope observation picture (with delamination marked) for pristine (a) and soaked-dried (b) LFP-CMC electrodes

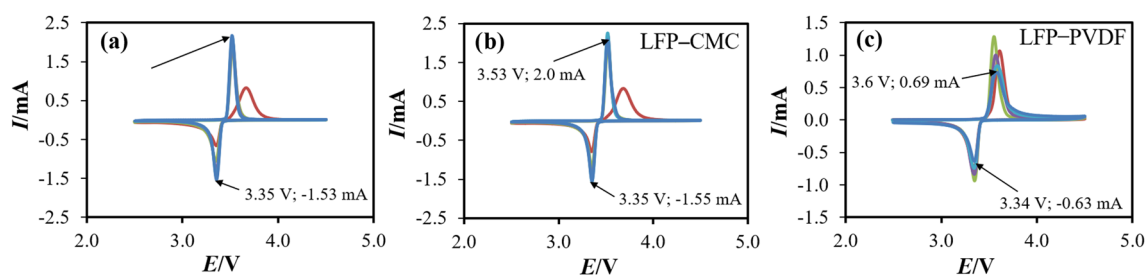
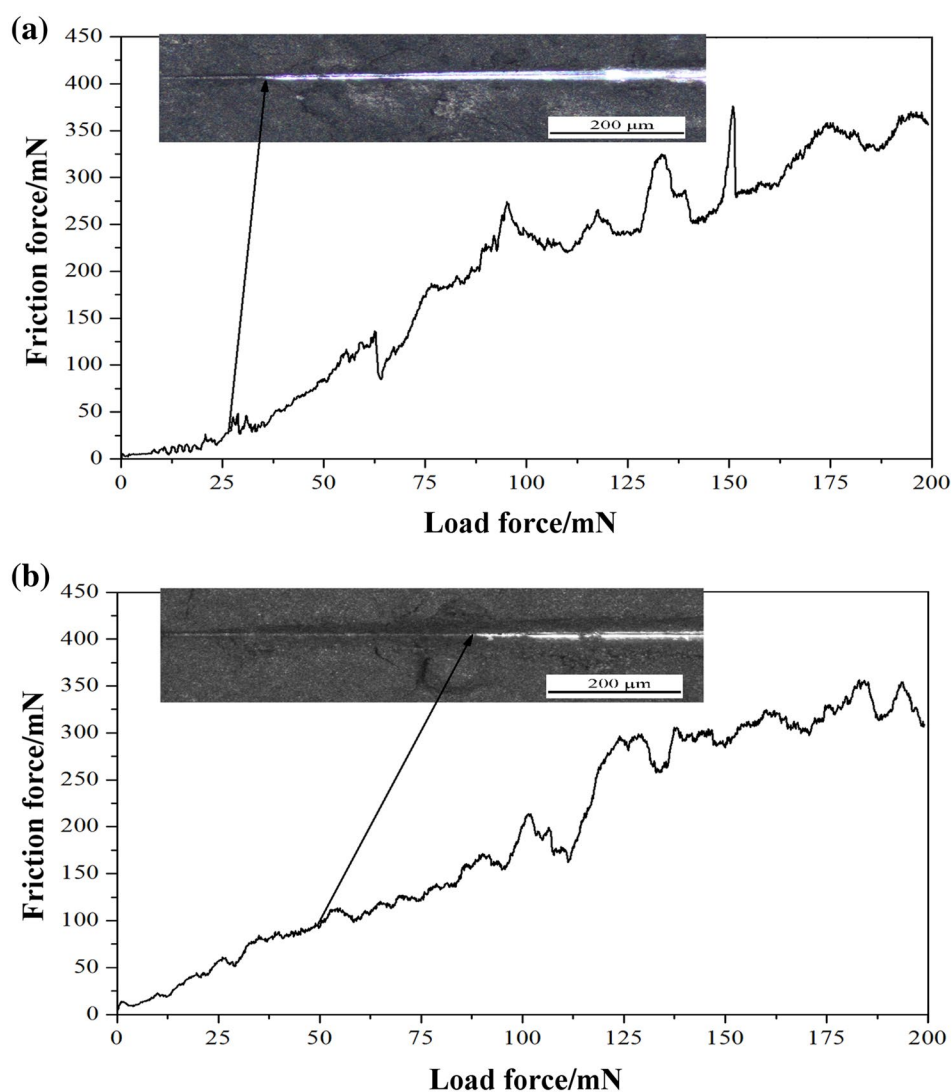


**Fig. 5** Cyclic voltammetry curves of first five cycles (1st—red, 2nd—green, 3rd—purple, 4th—light blue, 5th—dark blue) of LFP electrode with **a** LBG, **b** CMC, and **c** PVDF binder at scan rate of  $2 \text{ mV s}^{-1}$ . (Color figure online)

insertion/deinsertion process, which is visible in the next cycles [31, 32]. In the case of the electrode with PVDF as a binder, lower current peaks were observed after the second cycle, indicating electrochemical instability and deterioration of the interfacial charge transfer through the SEI. The

LFP-LBG electrode, similarly as the LFP-CMC electrode, showed a lower potential difference between redox peaks, and better cyclic reversibility and stability than those of PVDF. The small potential difference, higher current peaks, and a stable cyclic reversibility during cycling confirmed

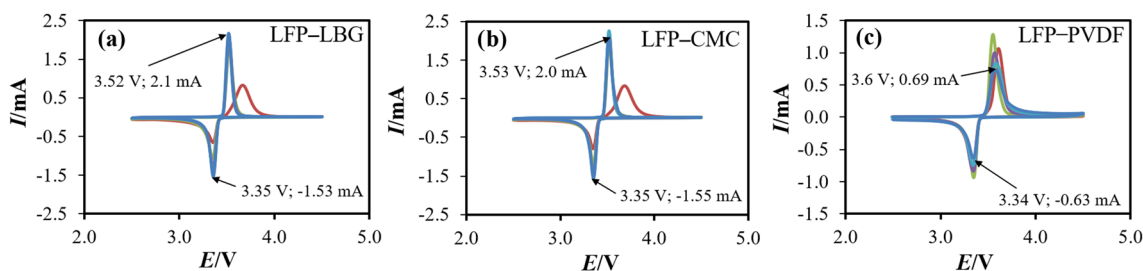


**Fig. 6** Cyclic voltammetry curves of first five cycles (1st—red, 2nd—green, 3rd—purple, 4th—light blue, 5th—dark blue) of LTO electrode with **a** LBG, **b** CMC, and **c** PVDF binder at scan rate of  $2 \text{ mV s}^{-1}$ . (Color figure online)

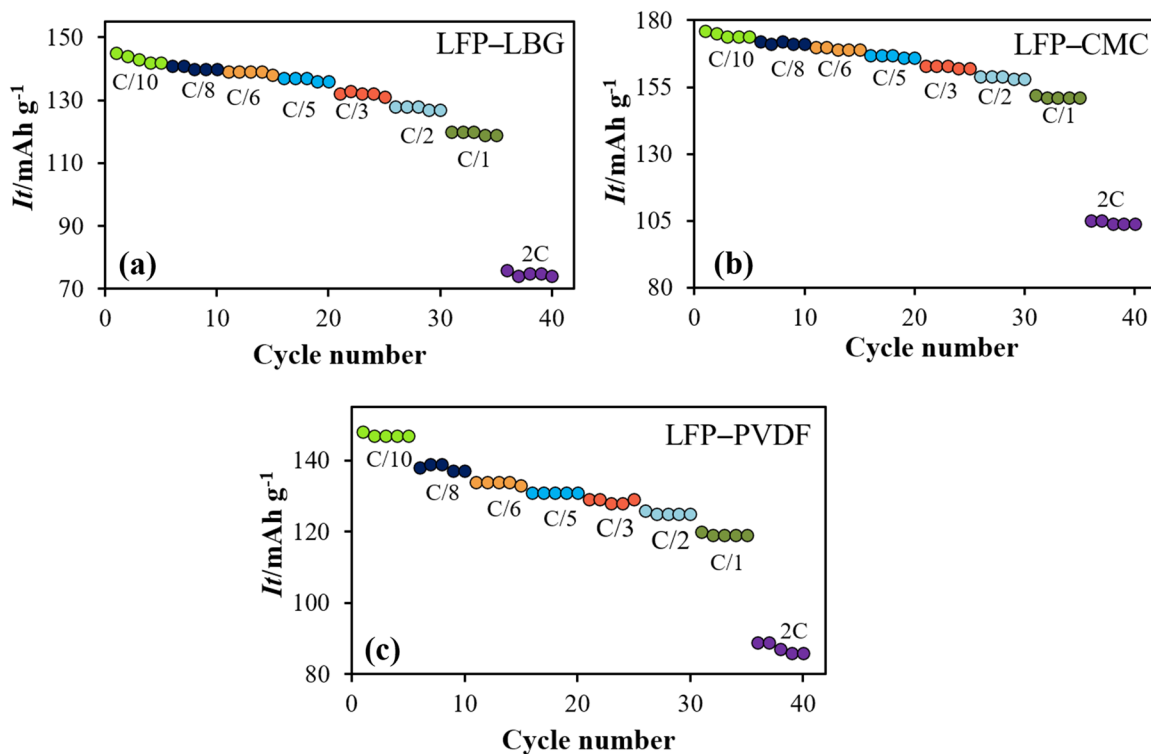
that the LFP-LBG electrode has a lower electrode polarization and better electrochemical kinetics than PVDF, similarly to CMC (Fig. 5).

Figure 6 presents cyclic voltammetry of LTO electrodes with different binders. For the LTO-LBG and LTO-CMC electrodes, the anodic and cathodic currents for peaks in the first cycle were lower and the potential difference between the peaks was higher than in their successive cycles. This indicates worse charge transfer on electrodes in the first cycle. Figure 6c gives the CV plot of LTO-PVDF, which in each subsequent cycle is characterized by a lower cathodic peak. For all LTO systems the results are similar. LTO electrodes with used binders showed stability during cycling and a comparable polarization [33].

### 3.5 Galvanostatic charging/discharging

Cycling performances of LFP-LBG, LFP-CMC, and LFP-PVDF electrodes are presented in Fig. 7a–c. Electrochemical characterization started with three charge/discharge cycles to form an effective surface layer that protects LFP from further reactions with the electrolyte.

Afterwards, LFP-LBG, LFP-CMC, and LFP-PVDF half-cells were galvanostatically discharged for 5 cycles at progressively increased currents (C/10, C/8, C/6, C/5, C/4, C/2, C/1). LFP-LBG and LFP-PVDF electrodes had comparable It values for C/1 at around  $120 \text{ mAh g}^{-1}$  but for the current



**Fig. 7** Rate performances of LFP electrode with **a** LBG, **b** CMC, and **c** PVDF binder

rate 2C was about  $10 \text{ mAh g}^{-1}$  higher for LFP–PVDF. In case of LFP, the capability for the CMC electrode is better than for the other electrodes as it is approx.  $174 \text{ mAh g}^{-1}$  and for LFP–LBG and LFP–PVDF electrodes gave It values of 142 and  $147 \text{ mAh g}^{-1}$  after the fifth cycle for the C/10 rate. For all LFP-binder systems, there were the greatest decrease of the It value for the 2C current. However, the It value was also the highest at 2C rate for the LFP–CMC electrode and was approximately equal about  $105 \text{ mAh g}^{-1}$ . The

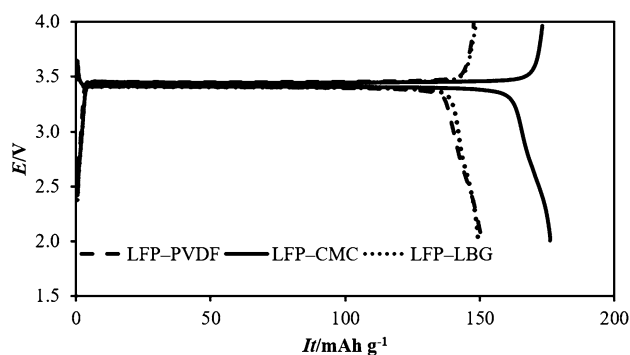


**Fig. 8** Galvanostatic charging/discharging curves of the LFP-Binder|1 M  $\text{LiPF}_6$  in EC:DMC (1:1 w/w)|Li cell. Cathode mass was ca. 2.5–3.5 mg, current C/10

charge–discharge voltage profiles of LFP–LBG, LFP–CMC, and LFP–PVDF electrodes at the charge–discharge rate of C/10 are given in Fig. 8. For all charging/discharging curves, the same potential plateau was recorded (3.4 V). This indicates that at C/10, diffusion of lithium ions in the electrodes with different binders is sufficient and does not limit the charging/discharging process. Transport of lithium ions between and inside particles is the main limitation of high current charging or discharging processes.

The LTO-binder|electrolyte|Li systems were charged/discharged at current rates ranging from C/10 to 2C (Fig. 9a–c). The cells that contain the CMC and PVDF binders showed higher It values under lower current rates (C/10), i.e., 179 and  $173 \text{ mAh g}^{-1}$ , in comparison to the cells containing the LBG binder, which demonstrated a discharge capacity of  $141 \text{ mAh g}^{-1}$ . The LTO electrodes with LBG used as a binder showed the highest It value at  $86 \text{ mAh g}^{-1}$  at a current density of 1 C, whereas those using CMC and PVDF as binders showed a capacity of only ca.  $50 \text{ mAh g}^{-1}$ . For the discharging rate 2C for the LTO–LBG electrode, there was a sudden decrease in the It value, but it was the highest value among the other electrodes and amounted to about  $50 \text{ mAh g}^{-1}$ .

The rate capability may be determined by calculating the percentage of the It value retained at a higher C-rate (2C)

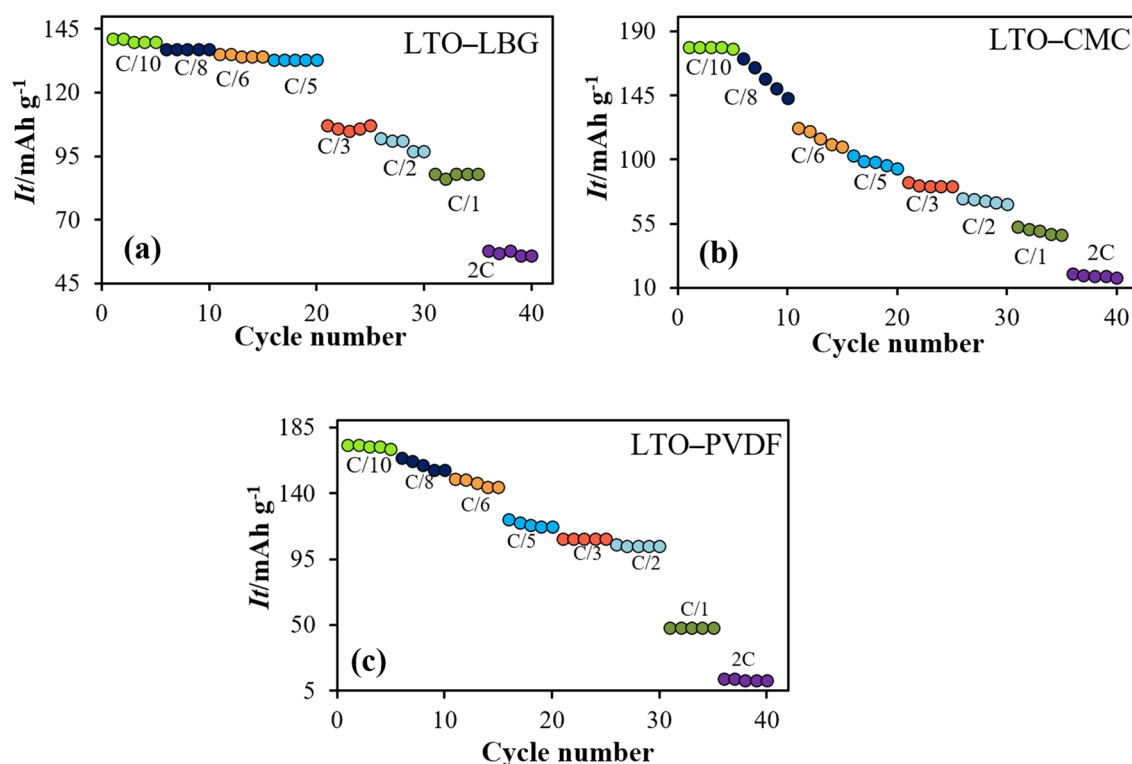


**Fig. 9** Rate performances of LTO electrode with **a** LBG, **b** CMC, and **c** PVDF binder



from the  $I_t$  value obtained at lower C-rates (C/10). For the electrodes with the LBG binder 40.0% of their  $I_t$  value is retained, while for electrodes with CMC and PVDF binders it is 8.3% and 5.8% of  $I_t$  value, respectively. At high rate, the electrode with the LBG binder, due to a porous structure with a strong network between the LTO particles and the conductive material, promotes diffusion of lithium ions, which leads to the improved rate capability as observed in comparison with the cells containing CMC and PVDF binders. However, a lower  $I_t$  value for the C/10 rate could be caused by partial blocking of the active material surface by the binder. Figure 10 shows charge–discharge curves of LTO–LBG, LTO–CMC, and LTO–PVDF electrodes at the charge–discharge rate of C/10. For all the charging–discharging curves the same potential plateau of ca. 1.65 V was recorded, which may suggest that at the C/10 rate the diffusion of lithium ions in electrodes with different binders is sufficient and does not limit the charging/discharging process. The charging–discharging voltage profiles differed in time relative to each other. In addition, you can see differences in the time for the charging and discharging process of the system with the PVDF electrode. This means that irreversible reactions may occur, which is unfavorable and may lead to a shorter life of the cell.

The data of the electrochemical performance at current rate C/5 of LFP cathodes and LTO anodes are summarized in Table 2. The state of health (SOH) of the LFP cathode is 78%, 77%, and 70% for LFP–CMC, LFP–LBG, and LFP–PVDF, respectively. The voltage profiles of the

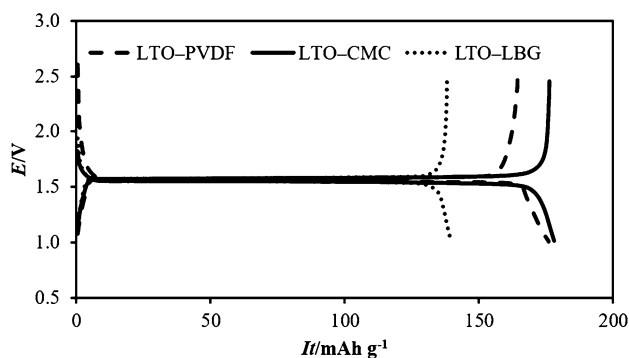


**Fig. 10** Galvanostatic charging/discharging curves of the LTO–Binder|1 M LiPF<sub>6</sub> in EC:DMC (1:1w/w)|Li cell. Anode mass was ca. 2.8–3.5 mg, current C/10

**Table 2** Electrochemical performance of LFP and LTO electrodes with different binders at current rate C/5

Electrode	LFP–LBG	LFP–CMC	LFP–PVDF	LTO–LBG	LTO–CMC	LTO–PVDF
Discharge capacity at 100th cycle (mAh g <sup>-1</sup> )	112	137	103	118	84	100
SOH* after 100 cycles (%)	77	78	70	74	46	56

\*The State of Health (SOH) estimated the maximum releasable capacity [34, 35]

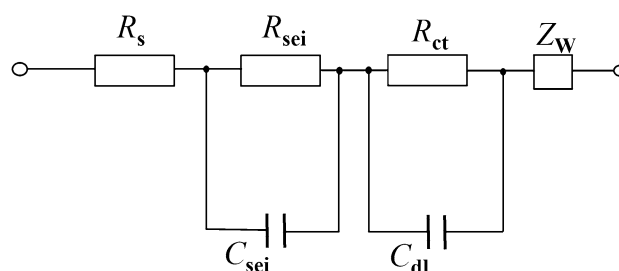
LTO anodes reveal that the SOH is 74% for LTO–LBG, 56% for LTO–PVDF, and 46% for LTO–CMC. The discharge capacity decreases for all the systems. The capacity after 100 cycles of the batteries with LFP cathode has the highest value for the system with CMC and of the cells with LTO anode the highest capacity presents the system with LBG. This result indicates that the electrodes with LBG binder maintain a good cycle performance.

### 3.6 Impedance studies

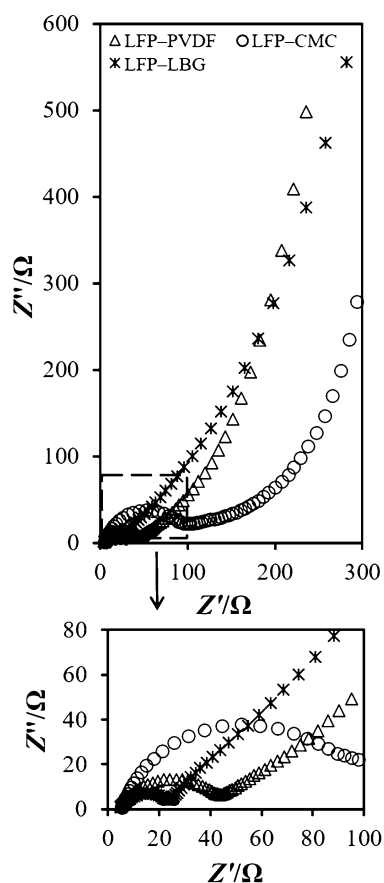
In the following sections, the results of impedance measurements on LFP–PVdF|Li, LFP–CMC|Li, LFP–LBG|Li and LTO–PVdF|Li, LTO–CMC|Li, LTO–LBG|Li cells are presented as a function of time. Electrochemical impedance spectroscopy was performed after galvanostatic charging, discharging, and again charging. The EIS data were quantitatively analyzed using an equivalent circuit model (Fig. 11) consisted of electrolyte resistance ( $R_s$ ) in series with two-time constants ( $R$  and  $C$  in parallel) and Warburg element  $Z_W$ . The two-time constants (RC) reflect solid electrolyte interphase resistance ( $R_{sei}$ ,  $C_{sei}$ ) and the charge transfer process which took place at electrode/electrolyte interphase ( $R_{ct}$ ,  $C_{dl}$ ) [36, 37]. The Warburg element is related to the diffusion of charged ions from the bulk of electrolyte to the surface of the electrode [38, 39]. The individual impedance parameters were determined by complex nonlinear least-square fits using the Zview2 software.

Figure 12 shows the impedance spectra of a LFP cathode with different binders taken at 298 K after 3 steps of galvanostatic charging/discharging.

Semi-circles are observed in the Nyquist plot, which is in good agreement with literature data [40]. The impedance



**Fig. 11** Equivalent circuit used for impedance spectra deconvolution



**Fig. 12** Impedance spectra of LFP–PVDF, LFP–CMC, and LFP–LBG cathodes taken at 298 K after 3 steps of galvanostatic charging/discharging, (after lithiation to 2.4 V). Counter electrode: lithium metal

obtained is not only from the LFP electrode, but also from the lithium counter electrode, as shown in the literature [36].

However, the value of charge current density suggests that it was mainly influenced by the LFP electrode. According to literature,  $j_0$  for lithium is of the order of  $10^{-10}$ – $10^{-1}$  mA cm $^{-2}$  [41–45]. Therefore, when comparing the results of the change in measured  $R_{ct}$  and  $R_{sei}$ , we connect mainly with the LFP electrode, not with lithium. For LFP–LBG and LFP–PVDF, the shape of the spectra is similar. The impedance spectra for the LFP–CMC/Li system are obviously different, as there are two semi-circles, the left corresponding to the passivated film on the electrode surface and the right semi-circle representing the charge transfer. The passivation film ( $R_{sei}$ ) and charge transfer ( $R_{ct}$ ) resistances obtained from the deconvolution are shown in Table 3.

$R_{sei}$  and  $R_{ct}$  given in ohms are expressed versus the geometrical surface area of electrodes (1.27 cm $^2$ ). It can be seen from Table 3 that resistance of the passivation film was 15  $\Omega$  for LFP–LBG, 32  $\Omega$  for LFP–PVDF, with the highest of 98  $\Omega$  for LFP–CMC, respectively. The values of charge transfer

**Table 3** Parameters of tested cathodes (expressed versus mass of active material): mass  $m$ , specific BET surface area, real surface area  $A$  calculated as  $m \times \text{BET}$ , resistance of electrolyte  $R_s$ , passivation film resistance  $R_{sei}$ , resistance of charge transfer process  $R_{ct}$ , exchange current density  $j_0$

	LFP–PVDF	LFP–CMC	LFP–LBG
$R_s/\Omega$	4.7	5.1	4.9
$R_{sei}/\Omega$	32	98	15
$R_{ct}/\Omega$	9.0	2.2	3.3
$m/\text{mg}$	2.6	3.0	2.8
$\text{BET}/\text{m}^2 \text{g}^{-1}$	15.4	15.4	15.4
$A/\text{cm}^2$	393	462	431
$A R_{ct}/\Omega \text{cm}^2$	3537	1016	1422
$j_0/\text{mA cm}^{-2}$	$0.73 \times 10^{-2}$	$2.53 \times 10^{-2}$	$1.80 \times 10^{-2}$

resistances  $R_{ct}$  were, respectively, 3.3  $\Omega$ , 9  $\Omega$ , and 2.2  $\Omega$ . Charge transfer resistances may be converted into surface areas independent of exchange current densities:

$$j_0 = \frac{RT}{FA} \frac{1}{R_{ct}} \quad (1)$$

All values are given in Table 3. The exchange current density for LFP–LBG is ca. two times higher than for LFP–PVDF. However,  $j_0$  obtained for all the three cathodes is in the range of  $0.73 \times 10^{-2}$  mA cm $^{-2}$  (LFP–PVDF) to  $2.53 \times 10^{-2}$  mA cm $^{-2}$  (LFP–CMC) and this is consistent with the literature data for the LFP cathode [33, 46]. This suggests that LBG as a binder works as effectively as PVDF, while it may even improve the kinetic parameters of electrode processes. The impedance spectra of an LTO anode with different binders taken at 298 K are shown in Fig. 13.

The Nyquist plots of the anodes were obtained after formation cycles, exhibiting one semi-circle in the high-frequency region and one slope in the low-frequency region.

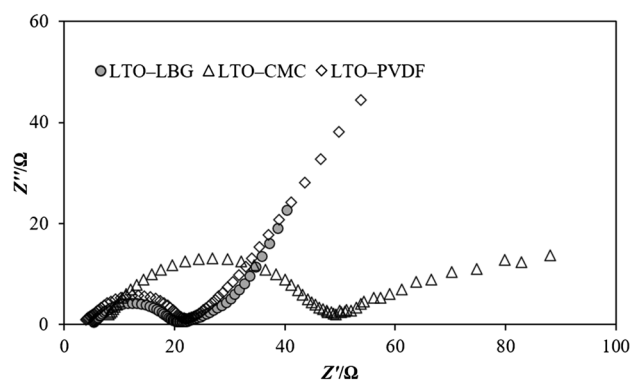


**Fig. 13** Impedance spectra of LTO–PVDF, LTO–CMC, and LTO–LBG anodes taken at 298 K after 3 steps of galvanostatic charging/discharging (after lithiation to 1.2 V). Counter electrode: lithium metal

**Table 4** Parameters of tested anodes (expressed versus mass of active material): mass  $m$ , specific BET surface area, real surface area  $A$  calculated as  $m \times \text{BET}$ , resistance of electrolyte  $R_s$ , passivation film resistance  $R_{\text{sei}}$ , resistance of charge transfer process  $R_{\text{ct}}$ , exchange current density  $j_0$

	LTO–PVDF	LTO–CMC	LTO–LBG
$R_s/\Omega$	1.9	3.0	5.0
$R_{\text{sei}}/\Omega$	15	41	16
$R_{\text{ct}}/\Omega$	4.3	4.6	3.2
$m/\text{mg}$	1.9	2.0	2.1
$\text{BET}/\text{m}^2 \text{ g}^{-1}$	32.6	32.6	32.6
$A/\text{cm}^2$	610	640	685
$A R_{\text{ct}}/\Omega \text{ cm}^2$	2623	2944	2192
$j_0/\text{mA cm}^{-2}$	$0.98 \times 10^{-2}$	$0.87 \times 10^{-2}$	$1.17 \times 10^{-2}$

The semi-circle in the high-frequency region corresponds to the impedance of Li-ion migration through the passivated film, while the semi-circle in the low-frequency region is ascribed to the impedance of charge transfer related to the electrode surface [13]. The linear slope at the low-frequency range corresponds to lithium-ion diffusion to the electrode surface. The LTO–LBG and LTO–PVDF electrodes exhibit similar shape of their spectra. The most striking difference is connected with resistance magnitude. The passivation film ( $R_{\text{sei}}$ ) and charge transfer ( $R_{\text{ct}}$ ) resistances obtained from the deconvolution procedure are shown in Table 4.

It can be seen that resistance of the passivation film was 16  $\Omega$  for LTO–LBG, 15  $\Omega$  for LTO–PVDF, while it was highest, at 41  $\Omega$ , for LTO–CMC. The values of charge transfer resistances  $R_{\text{ct}}$  were 4.8  $\Omega$ , 4.3  $\Omega$  and 3.2  $\Omega$ , respectively. Exchange current densities can be found in the literature for the  $\text{Li}_4\text{Ti}_5\text{O}_{12}$  material:  $j_0 = 5.9 \times 10^{-3} \text{ mA cm}^{-2}$  [47] and  $j_0 = 2.38 \times 10^{-4} \text{ mA cm}^{-2}$  [48]. However, a comparison of the present values with literature data is problematic because the real surface areas of electrodes were not reported. It suggests that the kinetics of charge transfer process occurring at the anode is also slower in comparison to metallic lithium, while the surface area is larger [49]. The LBG binder has a positive effect on the exchange current density, being the greatest among the compared binders.

## 4 Conclusions

In summary, LBG was used for the first time as an electrode binder. Its properties such as thermal stability, morphology, adhesive, and electrochemical properties were compared with those of the most popular binders from the group of water and organic-soluble binders. They were tested in the  $\text{LiLiFePO}_4$  and  $\text{LiLi}_4\text{Ti}_5\text{O}_{12}$  systems. The new binder (LBG) is environmentally friendly and is of natural origin. Locust bean gum has good thermal stability up to a

much higher temperature than required by Li-ion batteries. LFP–LBG electrodes have structural properties comparable to those of electrodes with a conventional binder (PVDF), while in the LTO–LBG system the binder ensures the electrical integrity of the network even after cycling, which leads to rapid electron migration between LTO particles and carbon black, as well as electrolyte diffusion in the electrode material exceeding that in the systems with CMC and PVDF as a binder. In addition, its electrochemical properties are promising for commercial use. Particularly noticeable is the reduction of charge transfer resistance and the improvement of kinetics in electrodes using LBG as the binder. It has been reported that charge transfer resistance for LFP electrodes with CMC and LBG are comparable (2.2  $\Omega$  and 3.3  $\Omega$ , respectively) and much lower than for PVDF (9  $\Omega$ ). In the case of the LTO electrode,  $R_{\text{ct}}$  is lower for the LBG binder amounting to 3.2  $\Omega$ , whereas for CMC and PVDF it is 4.6 and 4.3  $\Omega$ , respectively. This involves potential for obtaining higher power for Li-ion batteries solely by changing the binding material. This is evident in cyclic tests for different currents, where the  $I_t$  values obtained at a higher current regime change less for the systems with better kinetic parameters. For example, the LTO–LBG electrode in a half-cell has twofold higher  $I_t$  value at the C/1 and even more at 2C current rate compared to the systems with LTO–CMC and LTO–PVDF electrodes.

**Acknowledgements** This work was supported by the PUT Grant No. 03/31/DSMK/0363.

**Funding** Poznan University of Technology

**Open Access** This article is licensed under a Creative Commons Attribution 4.0 International License, which permits use, sharing, adaptation, distribution and reproduction in any medium or format, as long as you give appropriate credit to the original author(s) and the source, provide a link to the Creative Commons licence, and indicate if changes were made. The images or other third party material in this article are included in the article's Creative Commons licence, unless indicated otherwise in a credit line to the material. If material is not included in the article's Creative Commons licence and your intended use is not permitted by statutory regulation or exceeds the permitted use, you will need to obtain permission directly from the copyright holder. To view a copy of this licence, visit <http://creativecommons.org/licenses/by/4.0/>.

## References

1. Bitsch B, Dittmann J, Schmitt M et al (2014) A novel slurry concept for the fabrication of lithium-ion battery electrodes with beneficial properties. Elsevier, Amsterdam
2. Jeschull F, Brandell D, Wohlfahrt-Mehrens M, Memm M (2017) Water-soluble binders for lithium-ion battery graphite electrodes: slurry rheology, coating adhesion, and electrochemical performance. *Energy Technol* 5:2108–2118. <https://doi.org/10.1002/ente.201700200>

3. Kim GT, Jeong SS, Joost M et al (2011) Use of natural binders and ionic liquid electrolytes for greener and safer lithium-ion batteries. *J Power Sources* 196:2187–2194. <https://doi.org/10.1016/j.jpowsour.2010.09.080>
4. Prasanna K, Subburaj T, Jo YN et al (2015) Environment-friendly cathodes using biopolymer chitosan with enhanced electrochemical behavior for use in lithium ion batteries. *ACS Appl Mater Interfaces* 7:7884–7890. <https://doi.org/10.1021/am5084094>
5. Kumar A, Thomas R, Karan NK et al (2009) Structural and electrochemical characterization of pure LiFePO<sub>4</sub> and nanocomposite C-LiFePO<sub>4</sub> cathodes for lithium ion rechargeable batteries. *J Nanotechnol* 2009:1–10. <https://doi.org/10.1155/2009/176517>
6. Zeng S, Li L, Xie L et al (2017) Graphene-supported highly crosslinked organosulfur nanoparticles as cathode materials for high-rate, long-life lithium-sulfur battery. *Carbon N Y* 122:106–113. <https://doi.org/10.1016/j.carbon.2017.06.036>
7. Rosero-Navarro NC, Kinoshita T, Miura A et al (2017) Effect of the binder content on the electrochemical performance of composite cathode using Li<sub>6</sub>PS<sub>5</sub>Cl precursor solution in an all-solid-state lithium battery. *Ionics* 23:1619–1624. <https://doi.org/10.1007/s11581-017-2106-x>
8. Lewandowski A, Jakobczyk P (2016) Kinetics of NaCF<sub>x</sub> and LiCF<sub>x</sub> systems. *J Solid State Electrochem* 20:3367–3373. <https://doi.org/10.1007/s10008-016-3305-5>
9. Billot N, Günther T, Schreiner D et al (2020) Investigation of the adhesion strength along the electrode manufacturing process for improved lithium-ion anodes. *Energy Technol* 8:1801136. <https://doi.org/10.1002/ente.201801136>
10. Zhang W, He X, Pu W et al (2011) Effect of slurry preparation and dispersion on electrochemical performances of LiFePO<sub>4</sub> composite electrode. *Ionics* 17:473–477. <https://doi.org/10.1007/s11581-011-0560-4>
11. Li CC, Wang YW (2013) Importance of binder compositions to the dispersion and electrochemical properties of water-based LiCoO<sub>2</sub> cathodes. *J Power Sources* 227:204–210. <https://doi.org/10.1016/j.jpowsour.2012.11.025>
12. Chou SL, Pan Y, Wang JZ et al (2014) Small things make a big difference: binder effects on the performance of Li and Na batteries. *Phys Chem Chem Phys* 16:20347–20359. <https://doi.org/10.1039/c4cp02475c>
13. Lewandowski A, Swiderska-Mocek A, Rudnicka E, Jakobczyk P (2014) Capacity of graphene anode in ionic liquid electrolyte. *J Solid State Electrochem* 18:2781–2788. <https://doi.org/10.1007/s10008-014-2539-3>
14. Tamura T, Aoki Y, Ohsawa T, Dokko K (2011) Polyaniline as a functional binder for LiFePO<sub>4</sub> cathodes in lithium batteries. *Chem Lett* 40:828–830. <https://doi.org/10.1246/cl.2011.828>
15. Nguyen VH, Wang WL, Jin EM, Gu HB (2013) Impacts of different polymer binders on electrochemical properties of LiFePO<sub>4</sub> cathode. *Appl Surf Sci* 282:444–449. <https://doi.org/10.1016/j.apsusc.2013.05.149>
16. Hu S, Li Y, Yin J et al (2014) Effect of different binders on electrochemical properties of LiFePO<sub>4</sub>/C cathode material in lithium ion batteries. *Chem Eng J* 237:497–502. <https://doi.org/10.1016/j.cej.2013.08.119>
17. Chou SL, Gao XW, Wang JZ et al (2011) Tin/polypyrrole composite anode using sodium carboxymethyl cellulose binder for lithium-ion batteries. *Dalton Trans* 40:12801–12807. <https://doi.org/10.1039/c1dt10396b>
18. He J, Zhong H, Wang J, Zhang L (2017) Investigation on xanthan gum as novel water soluble binder for LiFePO<sub>4</sub> cathode in lithium-ion batteries. *J Alloys Compd* 714:409–418. <https://doi.org/10.1016/j.jallcom.2017.04.238>
19. Bigoni F, De Giorgio F, Soavi F, Arbizzani C (2017) Sodium alginate: a water-processable binder in high-voltage cathode formulations. *J Electrochem Soc* 164:A6171–A6177. <https://doi.org/10.1149/2.0281701jes>
20. Liu J, Zhang Q, Wu ZY et al (2014) A high-performance alginate hydrogel binder for the Si/C anode of a Li-ion battery. *Chem Commun* 50:6386–6389. <https://doi.org/10.1039/c4cc00081a>
21. Lin C, Tang A, Mu H et al (2015) Aging mechanisms of electrode materials in lithium-ion batteries for electric vehicles. *J Chem* 2015. <https://doi.org/10.1155/2015/104673>
22. Maleki H, Deng G, Anani A, Howard J (1999) Thermal stability studies of Li-ion cells and components. *J Electrochem Soc* 146:3224–3229. <https://doi.org/10.1149/1.1392458>
23. Koo B, Kim H, Cho Y et al (2012) A highly cross-linked polymeric binder for high-performance silicon negative electrodes in lithium ion batteries. *Angew Chem Int Ed* 51:8762–8767. <https://doi.org/10.1002/anie.201201568>
24. Dionísio M, Grenha A (2012) Locust bean gum: exploring its potential for biopharmaceutical applications. *J Pharm Bioallied Sci* 4:175–185. <https://doi.org/10.4103/0975-7406.99013>
25. Batal H, El, Hasib A (2012) Revue de Génie Industriel Rheology and influence factor of Locust Bean Gum solution, pp 55–62
26. Jow TR, Ding MS, Xu K et al (2003) Nonaqueous electrolytes for wide-temperature-range operation of Li-ion cells. *J Power Sources* 119–121:343–348. [https://doi.org/10.1016/S0378-7753\(03\)00153-8](https://doi.org/10.1016/S0378-7753(03)00153-8)
27. Du Pasquier A, Plitz I, Menocal S, Amatucci G (2003) A comparative study of Li-ion battery, supercapacitor and nonaqueous asymmetric hybrid devices for automotive applications. *J Power Sources* 115:171–178. [https://doi.org/10.1016/S0378-7753\(02\)00718-8](https://doi.org/10.1016/S0378-7753(02)00718-8)
28. Sabbah R, Kizilel R, Selman JR, Al-Hallaj S (2008) Active (air-cooled) vs. passive (phase change material) thermal management of high power lithium-ion packs: limitation of temperature rise and uniformity of temperature distribution. *J Power Sources* 182:630–638. <https://doi.org/10.1016/j.jpowsour.2008.03.082>
29. Chen J, Liu J, Qi Y et al (2013) Unveiling the roles of binder in the mechanical integrity of electrodes for lithium-ion batteries. *J Electrochem Soc* 160:A1502–A1509. <https://doi.org/10.1149/2.088309jes>
30. Martha SK, Markevich E, Burgel V et al (2009) A short review on surface chemical aspects of Li batteries: a key for a good performance. *J Power Sources* 189:288–296. <https://doi.org/10.1016/j.jpowsour.2008.09.084>
31. Peled E, Yamin H (1979) Solid electrolyte interphase (SEI) electrodes. Part I. The kinetics of lithium in LiAlCl<sub>4</sub>-SOCl<sub>2</sub>. *Isr J Chem* 18:131–135. <https://doi.org/10.1002/ijch.197900016>
32. Levi MD, Aurbach D (1997) Simultaneous measurements and modeling of the electrochemical impedance and the cyclic voltammetric characteristics of graphite electrodes doped with lithium. *J Phys Chem B* 101:4630–4640. <https://doi.org/10.1021/jp9701909>
33. Zhong S, Wu L, Liu J (2012) Sol-gel synthesis and electrochemical properties of 9LiFePO<sub>4</sub>-Li<sub>3</sub>V<sub>2</sub>(PO<sub>4</sub>)<sub>3</sub>/C composite cathode material for lithium ion batteries. *Electrochim Acta* 74:8–15. <https://doi.org/10.1016/j.electacta.2012.03.181>
34. Ng KS, Moo CS, Chen YP, Hsieh YC (2009) Enhanced coulomb counting method for estimating state-of-charge and state-of-health of lithium-ion batteries. *Appl Energy* 86:1506–1511. <https://doi.org/10.1016/j.apenergy.2008.11.021>
35. Murnane M, Ghazel A (2017) A Closer Look at State of Charge (SOC) and State of Health (SOH) Estimation Techniques for Batteries. Analog devices
36. Hanai K, Ueno M, Imanishi N et al (2011) Interfacial resistance of the LiFePO<sub>4</sub>-C/PEO-LiTFSI composite electrode for dry-polymer lithium-ion batteries. *J Power Sources* 196:6756–6761. <https://doi.org/10.1016/j.jpowsour.2010.10.079>
37. Lewandowski A, Biegun M, Galinski M (2012) Kinetics of Li + reduction in 1-methyl-3-propylpiperidinium



- bis(trifluoromethylsulfonyl) imide room temperature ionic liquid. *Electrochim Acta* 63:204–208. <https://doi.org/10.1016/j.electacta.2011.12.100>
38. (2012) The modified inductance element La, EC-Lab – Application Note #42 08/2012. 4 Rue de Vaucanson, 38170 Seyssinet-Pariset, FRANCE
  39. Ryl J, Bogdanowicz R, Slepski P et al (2014) Dynamic electrochemical impedance spectroscopy (deis) as a tool for analyzing surface oxidation processes on boron-doped diamond electrodes. *J Electrochem Soc* 161:0–7. <https://doi.org/10.1149/2.016406jes>
  40. Song JY, Lee HH, Wang YY, Wan CC (2002) Two- and three-electrode impedance spectroscopy of lithium-ion batteries. *J Power Sources* 111:255–267
  41. Lee SI, Jung UH, Kim YS et al (2002) A study of electrochemical kinetics of lithium ion in organic electrolytes. *Korean J Chem Eng* 19:638–644. <https://doi.org/10.1007/BF02699310>
  42. Nagasubramanian G, Attia AI, Halpert G (1994) A polyacrylonitrile-based gelled electrolyte: electrochemical kinetic studies. *J Appl Electrochem* 24:298–302. <https://doi.org/10.1007/BF00242056>
  43. Munichandraiah N, Shukla AK, Scanlon LG, Marsh RA (1996) On the stability of lithium during ageing of Li/PEO8LiClO4/Li cells. *J Power Sources* 62:201–206. [https://doi.org/10.1016/S0378-7753\(96\)02426-3](https://doi.org/10.1016/S0378-7753(96)02426-3)
  44. Wang XM, Nishina T, Uchida I (1997) Application of the micro-electrode technique to the kinetic study of lithium deposition/dissolution and alloying in organic solutions. *J Power Sources* 68:483–486. [https://doi.org/10.1016/S0378-7753\(97\)02522-6](https://doi.org/10.1016/S0378-7753(97)02522-6)
  45. Liebenow C, Lühder K (1996) Electrochemical characterization of polymer precoated lithium electrodes. *J Appl Electrochem* 26:689–692. <https://doi.org/10.1007/BF00241509>
  46. Cao J, Qu Y, Guo R (2012) La 0.6Sr 0.4CoO 3- $\delta$  modified LiFePO 4/C composite cathodes with improved electrochemical performances. *Electrochim Acta* 67:152–158. <https://doi.org/10.1016/j.electacta.2012.02.031>
  47. Shao D, He J, Luo Y et al (2012) Synthesis and electrochemical performance of nanoporous Li 4Ti 5O 12 anode material for lithium-ion batteries. *J Solid State Electrochem* 16:2047–2053. <https://doi.org/10.1007/s10008-011-1604-4>
  48. Medina PA, Zheng H, Fahlman BD et al (2015) Li4Ti5O12/graphene nanoribbons composite as anodes for lithium ion batteries. *Springerplus* 4:1–7. <https://doi.org/10.1186/s40064-015-1438-0>
  49. Swiderska-Mocek A, Lewandowski A (2017) Kinetics of Li-ion transfer reaction at LiMn2O4, LiCoO2, and LiFePO4 cathodes. *J Solid State Electrochem* 21:1365–1372. <https://doi.org/10.1007/s10008-016-3499-6>

**Publisher's Note** Springer Nature remains neutral with regard to jurisdictional claims in published maps and institutional affiliations.

## Affiliations

Paweł Jakóbczyk<sup>1,2</sup>  · Michał Bartmański<sup>3</sup> · Ewelina Rudnicka<sup>1</sup>

<sup>1</sup> Faculty of Chemical Technology, Poznan University of Technology, Berdychowo 4, 60 965 Poznan, Poland

<sup>2</sup> Department of Metrology and Optoelectronics, Faculty of Electronics, Telecommunications and Informatics, Gdańsk University of Technology, Gabriela Narutowicza 11/12, 80-233 Gdańsk, Poland

<sup>3</sup> Department of Materials Engineering and Bonding, Faculty of Mechanical Engineering, Gdańsk University of Technology, Gabriela Narutowicza 11/12, 80-233 Gdańsk, Poland